arXiv:1701.03646v1 [physics.chem-ph] 13 Jan 2017

High-resolution spectroscopy of He_2^+ using Rydberg-series extrapolation and Zeeman-decelerated supersonic beams of metastable He_2

Paul Jansen, Luca Semeria, Frédéric Merkt*

Laboratory of Physical Chemistry, ETH Zurich, CH-8093 Zurich, Switzerland

Abstract

Recently, high-resolution spectroscopy of slow beams of metastable helium molecules (He_2^*) generated by multistage Zeeman deceleration was used in combination with Rydberg-series extrapolation techniques to obtain the lowest rotational interval in the molecular helium ion at a precision of 18 MHz [Jansen *et al.* Phys. Rev. Lett. 115 (13) (2015) 133202], limited by the temporal width of the Fourier-transform-limited laser pulses used to record the spectra. We present here an extension of these measurements in which we have (1) measured higher rotational intervals of He_2^+, (2) replaced the pulsed UV laser by a cw UV laser and improved the resolution of the spectra by a factor of more than five, and (3) studied M_J redistribution processes in regions of low magnetic fields of the Zeeman decelerator and shown how these processes can be exploited to assign transitions originating from specific spin-rotational levels (N'', J'') of He_2^*.

Keywords: High-Resolution Spectroscopy, Molecular Rydberg States, Zeeman Deceleration, Metastable Helium Molecules.

2015 MSC: 00-01, 99-00

1. Introduction

Translationally cold samples of molecules offer interesting perspectives for high-resolution spectroscopy. The long measurement times that are possible

*merkt@phys.chem.ethz.ch

with such samples and the reduced Doppler widths are ideally suited for precision measurements of transition frequencies in molecules, and such measurements are beginning to be relevant in the context of tests of the standard model of particle physics and some of its extensions [1]. Precision measurements in few-electron, light molecules such as H_2^+, H_2 and He_2^+ are used as tests of *ab initio* quantum-chemical calculations which aim at an exact solution of the Schrödinger equation and a rigorous determination of relativistic and quantum-electrodynamics (QED) corrections [2, 3, 4, 5, 6]. In these molecules, the velocity of the electrons is relatively low, and nonrelativistic quantum-electrodynamics turns out to be particularly successful. In this approach, the energy is expressed as a series expansion in powers of the fine-structure constant α, which is a measure of the classical electron speed

$$E(\alpha) = \mathcal{E}^{(0)} + \alpha^2\mathcal{E}^{(2)} + \alpha^3\mathcal{E}^{(3)} + \alpha^4\mathcal{E}^{(4)} + \mathcal{O}\left(\alpha^5\right). \tag{1}$$

The terms in different powers of α are associated with different contributions to the overall energy. $\mathcal{E}^{(0)}$ contains the Born-Oppenheimer energy including adiabatic and nonadiabatic interactions, while $\alpha^2\mathcal{E}^{(2)}$ and $\alpha^3\mathcal{E}^{(3)}$ represent the relativistic and leading-order QED corrections. Higher powers of α are associated with higher-order QED corrections. Recent calculations for the molecular hydrogen ion include relativistic and QED corrections up to terms proportional to α^6 and report an accuracy of 2 kHz for the first vibrational intervals of H_2^+ [3] and HD^+ [6]. The most accurate calculations of the energies in H_2, HD, and D_2 include full corrections up to terms proportional to α^3 as well as the dominant one-loop contribution of the α^4 term [4, 5]. The reported uncertainties are less than 30 MHz and the calculated and experimental results agree within this uncertainty [7, 8]. The best calculations of the rovibrational levels of He_2^+ [9] have an accuracy of about 120 MHz, sufficient to reproduce the energy-level structure measured in earlier experiments [10, 11], although they do not include relativistic and radiative corrections.

Few-electron diatomic molecules present experimental challenges for high-resolution studies of their spectra, and experimental data on their energy-level

structures are scarce. Indeed, the symmetric isotopomers do not have a permanent electric dipole moment, which implies that these species do not have a pure rotational nor a rovibrational spectrum. Spectroscopic data on the molecular helium cation are limited to rotational and vibrational transitions in the asymmetric $^3He^4He^+$ isotopomer reported by Yu *et al.* [10, 11] and microwave transitions between highly excited vibrational levels of the electronic ground state and the lowest vibrational levels of the first electronically excited states in $He_2{}^+$ by Carrington *et al.* [12]. The only experimental data available on the low-lying rovibrational levels of $^4He_2{}^+$ have been obtained by photoelectron spectroscopy [13] and from the Rydberg spectrum of He_2 using Rydberg-series extrapolation techniques [14, 15, 13, 16, 17].

The work presented in this article is devoted to measurements of the energy level structure of $He_2{}^+$ by high-resolution spectroscopy of Rydberg states of He_2 and extrapolation of the Rydberg series [13, 16, 17]. The strength of our approach to study $He_2{}^+$ relies on the facts that (1) its energy levels structure is obtained by extrapolation of allowed electronic transitions of He_2 in the ultraviolet (UV) range of the electromagnetic spectrum, (2) the initial state of He_2 we use, the metastable $a\,^3\Sigma_u^+$ state (called He_2^* hereafter), can easily be generated in supersonic beams, (3) He_2^* has a magnetic moment of two Bohr magneton, which makes it possible to decelerate He_2^* beams to low velocities in the laboratory reference frame using the technique of multistage Zeeman deceleration [18, 19], and (4) the electronic spectrum of He_2^* is well known and information on low-lying Rydberg states and fine-structure intervals facilitates the interpretation of spectra of high Rydberg states. We believe that, in the long term, these advantages will enable us to reach a higher precision and accuracy than currently possible in H_2 [7, 8, 20].

The spectrum of He_2 has been investigated exhaustively after its first detection in 1913, independently by Curtis [21] and Goldstein [22]. Most information about the Rydberg states of He_2 has been obtained with classical emission grating spectroscopy in the extensive measurements of Ginter and coworkers [23, 24, 25, 26, 27, 28, 29, 30, 15]. In addition, low-lying Rydberg states have

been investigated using infrared emission [31] and absorption [32] spectroscopy, laser-induced fluorescence spectroscopy [33], Fourier-transform emission spectroscopy [34, 35, 36, 37], laser absorption spectroscopy [38, 39, 40, 41], optical heterodyne concentration-modulation spectroscopy [42], and infrared emission spectroscopy from proton-irradiated cryogenic helium gas [43, 44]. Highly accurate measurements of the fine structure in the lowest rotational states of He_2^* ($\nu'' = 0$) have been performed by Lichten *et al.* using molecular-beam radio-frequency (r.f.) spectroscopy [45, 46, 47]. Bjerre and coworkers [40, 48, 41] employed laser-r.f. double-resonance spectroscopy to extend the measurements of the fine-structure intervals to higher rotational and vibrational states. Focsa *et al.* [36] performed a global fit on infrared and r.f. data to obtain a consistent set of molecular constants for the six lowest excited electronic states of He_2.

The structure of this article is as follows: After an overview of current knowledge on He_2^*, on the triplet Rydberg states of He_2, and on the ground state of He_2^+ in section 2, we summarize our experimental approach in section 3. The experimental results are presented in section 4 and a brief summary is provided in the conclusions section.

2. Energy levels of He_2 and He_2^+: general considerations

The van-der-Waals interaction between two helium atoms in their $^1S_0$ ground state is extremely weak and gives rise to a very shallow potential-energy well for the ground state of He_2, with a depth in the order of $10^{-3}\,cm^{-1}$ [49] and a single bound rovibrational state with a mean internuclear distance of almost 5 nm [50]. In contrast, He_2^+ in its $X^+\,^2\Sigma_u^+$ ground state is covalently bound, with a well depth of almost 2.5 eV [9]. The strongly bound nature of the He_2^+ ground state implies the existence of singlet and triplet Rydberg series of He_2. Many Rydberg states are known for He_2 that all belong to series converging on the $X^+\,^2\Sigma_u^+$ electronic ground state of He_2^+ [51, 52, 15]. With the exception of the single bound level of the electronic ground state, all bound states of He_2 are Rydberg states, so that He_2 can be regarded as a Rydberg molecule [53].

2.1. Metastable helium molecules He_2^*

The lowest Rydberg states of He_2, the $a\,^3\Sigma_u^+$ state, is metastable, with a calculated radiative lifetime of 18 s [54], because radiative decay to the ground electronic state is spin forbidden. Its long lifetime and the ease with which it can be produced in electric discharges make He_2^* an ideal initial state to study the electronic spectrum and the photoionization of He_2, as demonstrated in the numerous studies cited in the introduction. The triplet nature of He_2^* gives rise to a magnetic moment of two Bohr magneton and thus to an electron-Zeeman effect that can be exploited to slow down supersonic beams of He_2 by multistage Zeeman deceleration [19, 17] (see also Sections 3 and 4).

The generalized Pauli principle requires the total wavefunction to be symmetric under exchange of the two bosonic $^4He^{2+}$ ($I = 0$) nuclei, so that only rotational states for which the quantum number N (N is the quantum number associated with the total angular momentum excluding spin) is odd are allowed in states of Σ_u^+ symmetry, such as the $a\,^3\Sigma_u^+$ state of $^4He_2$ and the $X^+\,^2\Sigma_u^+$ state of $He_2{}^+$. The rotational and fine structure in the vibrational ground state of He_2^* can be described by an effective Hamiltonian [55, 56] appropriate to Hund's case (b) molecules in electronic states of Σ symmetry

$$H = B_0\vec{N}^2 - D_0\vec{N}^4 + H_0\vec{N}^6 + \tfrac{2}{3}\lambda_0\left(3S_z^2 - \vec{S}^2\right) + \gamma_0\vec{S}\cdot\vec{N}, \qquad (2)$$

where B_0 is the rotational constant, D_0 and H_0 are the quartic and sextic centrifugal distortion constants, λ_0 is the spin-spin interaction constant, γ_0 is the spin-rotation interaction constant, and $\vec{N}$ and $\vec{S}$ are the total angular momentum excluding spin and the total electron spin, respectively. The spin-spin and spin-rotation interactions split each rotational state N into three fine-structure components with total angular momentum quantum number $J = N, N \pm 1$. Levels of the same J value but N values differing by 2 mix under the influence of the spin-spin interaction. Matrix elements of Eq. (2) can be found in Ref. [56]. The fine-structure splittings of the three lowest rotational states in He_2 ($a\,^3\Sigma_u^+$ $\nu = 0$) are shown on the left-hand side of Fig. 1.

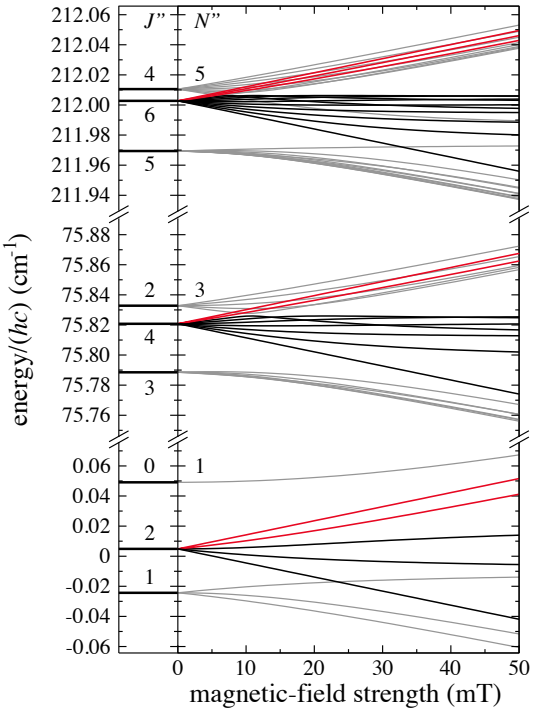

Figure 1: Fine structure (left panel) and Zeeman effect (right panel) of the $N'' = 1, 3$, and 5 states of He_2^*. The low-field-seeking magnetic sublevels of the $J'' = N'' + 1$ manifold are shown in red and states of the $J'' = N''$ and $N'' - 1$ are shown in grey.

To treat the effects of an external magnetic field, one needs two additional terms in the Hamiltonian

$$H_Z = -\frac{g_e \mu_B}{\hbar} \vec{S} \cdot \vec{B} - \frac{g_R \mu_B}{\hbar} \vec{N} \cdot \vec{B}, \tag{3}$$

where $g_e \approx -2.00232$ and g_R denote the electron and rotational g-factors, respectively. The second term on the right-hand side of Eq. (3) represents the coupling of the overall rotation of the molecule to the external magnetic field. This coupling is four orders of magnitude weaker than the coupling of the electron spin to the field and plays a negligible role for the deceleration experiments described below. On the right-hand side of Fig. 1, we show the eigenvalues of the combined Hamiltonian as a function of the magnetic-field strength for the three lowest rotational states in He_2^*. The Zeeman effect in higher rotational

states is almost identical to that for $N = 5$ because the fine structure at zero field only slowly changes with N at high N values and the rotational spacings are much larger than the Zeeman shifts, even for magnetic-field strengths of several Tesla [19].

2.2. He_2^+ and He_2 Rydberg states

In the $X^+\,^2\Sigma_u^+$ electronic ground state, the rotational structure of He_2^+ can also be described by Eq. (2). However, only the spin-rotation interaction [last term on the right-hand side of Eq. (2)] contributes to the fine structure, because there is only one unpaired electron. The spin-rotation interaction in the $X^+\,^2\Sigma_u^+$ state of He_2^+ splits each rotational state N^+ into two fine-structure states with $J^+ = N^+ \pm \frac{1}{2}$. In the following, we denote quantum numbers and molecular constants of the $a\,^3\Sigma_u^+$ state of He_2 and the $X^+\,^2\Sigma_u^+$ state of He_2^+ with double primed symbols and a "+" superscript, respectively, to avoid confusion. The splitting between the two J^+ states of a given N^+ value is given by $\gamma_0^+(N^+ + \frac{1}{2})$, where γ_0^+ is the spin-rotation coupling constant of the vibrational ground state of He_2^+ ($X^+\,^2\Sigma_u^+$ $\nu^+ = 0$).

Although γ_0^+ has not been measured for He_2^+ yet, one can estimate it to be ≈ -3 MHz from the known spin-rotation coupling constant in $^3He^4He^+$ [11] and the fact that γ_0^+ scales as μ^{-1} [57], where μ is the reduced mass of the molecule. To resolve the two fine-structure levels of the rotational states of He_2^+ with N^+ values greater than 9 and 51, an experimental resolution of 25 and 150 MHz, respectively, would be required.

The energy-level structure of low-lying Rydberg states of He_2 is adequately described by Hund's angular-momentum coupling case (b) and thorough analyses of many of these low-lying states have been reported (see references cited in the introduction). Rydberg states of high principal quantum number are more conveniently described by Hund's angular-momentum coupling case (d). The Rydberg series of He_2 that can be accessed from He_2^* by single-photon excitation are $np\sigma\ ^3\Sigma_g^+$ and $np\pi\ ^3\Pi_g^\pm$ in Hund's case (b) notation and npN_N^+ in Hund's case (d) notation. The two angular-momentum coupling schemes are related

by a unitary angular-momentum frame transformation with which rotational-electronic interactions are treated in the realm of multichannel quantum-defect theory [58]. The high-n states we use to extrapolate the series and determine the rotational energy-level structure of He_2^+ are best described in Hund's angular-momentum coupling case (d), as illustrated schematically in Fig. 2. Three np series converge on each rotational level N^+ of He_2^+, with N values of N^+ and $N^+ \pm 1$ ($\vec{N} = \vec{N}^+ + \vec{\ell}$, with $\ell = 1$ for p series). The series with $N = N^+$ have pure Hund's case (b) $np\pi\ ^3\Pi_g^-$ character and those with $N = N^+ \pm 1$ and $N > 1$ have mixed $np\sigma\ ^3\Sigma_g^+$ and $np\pi\ ^3\Pi_g^+$ character.

Because N, and not N^+, is the good quantum number, levels of the same N value that converge on different rotational states of He_2^+ interact, giving rise to spectral perturbations below and to rotational autoionization above the $N^+ = N - 1$ thresholds. These interactions, indicated by horizontal arrows in Fig. 2, couple series differing in N^+ by 2 and need to be accounted for in the extrapolation of the Rydberg series. The best way to do so is by using multichannel quantum-defect theory as implemented by Jungen [58]. In our determination of the lowest rotational interval of He_2^+ we extrapolated the series using the quantum defect parameters of the np triplet states of He_2 reported by Sprecher *et al.* [16]. If the positions of the rotational levels of the cation are not known with sufficient precision, as is the case for the series converging to the $N^+ = 11$ and 13 ionic levels discussed in Section 4, the series limits can be extrapolated in first approximation using Rydberg's formula

$$hc\tilde{\nu}_{n\ell} = E_{\rm I}\left(He_2^*\right) + E_{\rm rv}\left(He_2^+\right) - \frac{hc\mathcal{R}_{He_2}}{(n-\delta_\ell)^2}, \qquad (4)$$

where $\tilde{\nu}_{n\ell}$ represents the spectral position of the Rydberg states of principal and orbital angular-momentum quantum numbers n and ℓ, respectively, and quantum defect δ_ℓ. The quantities $E_{\rm I}(He_2^*)$, $E_{\rm rv}(He_2^+)$ and $\mathcal{R}_{He_2}$ represent the adiabatic ionization energy of He_2^*, the rovibrational energy of the He_2^+ ion core, and the mass-corrected Rydberg constant for He_2, respectively. Rydberg's formula adequately describes the noninteracting $npN^+_{N=N^+}$ series and also gives good extrapolation results for the other two series if states of very high n values

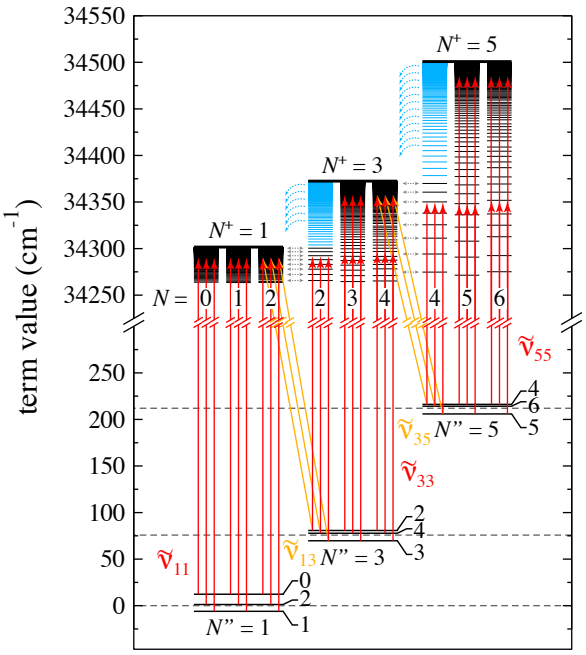

Figure 2: Energy-level diagram showing the rotational levels of He_2^* and the triplet np Rydberg states of He_2 that converge to the three lowest rotational levels of He_2^+. The positions of pure rotational levels of the metastable state are marked by dashed horizontal lines. The spin-rotation fine structure is exaggerated for clarity. Solid and dashed arrows indicate optically allowed transitions and channel interactions, respectively. Rapidly autoionizing levels are drawn in blue.

are used in the extrapolation.

The spin-spin coupling of the triplet Rydberg states of He_2 scales with n^{-3} and becomes negligible at high n values. The spin-rotation interaction is primarily that of the ion core, so that the fine structure converges to the spin-rotation splitting of He_2^+ at high values of n (see Fig. 6 of Ref. [59]).

The rotational selection rules for single-photon excitation from He_2^* to $np\sigma\,^3\Sigma_g^+$ and $np\pi\,^3\Pi_g^\pm$ Rydberg states are given by $N - N'' = 0, \pm 1$. Combined with the $\Delta\ell = \pm 1$ selection rule for transitions between Rydberg states, the overall selection rule for single-photon excitation from the $a\,^3\Sigma_u^+$ state to Rydberg levels converging to the $X^+\,^2\Sigma_u^+$ state is given by $\Delta N = N^+ - N'' = 0, \pm 2$. Transi-

tions from He_2^* to np Rydberg levels can therefore be unambiguously labeled as $N''_{J''} \rightarrow n\mathrm{p}N^+_N$. Transitions to Rydberg states with $\Delta N = 0, -2$, and $+2$ are referred to as Q(N'')-type, O(N'')-type, and S(N'')-type transitions, respectively. The Q-type transitions are far stronger than the O- and S-type transitions because the $He_2{}^+$ ion core is left with an electron hole of mainly s character after excitation of He_2 to np Rydberg states [60]. However, O-type transitions can gain intensity through rotational channel interactions between levels converging on different rotational states of the ion discussed above and indicated by the horizontal dashed arrows in Fig. 2. The observation of these O-type transitions in He_2 is essential for the determination of the relative positions of energy levels in both the metastable state and ion ground state.

3. Experimental setup and procedure

A schematic view of the laser systems and the experimental setup is shown in Fig. 3. In the experiments, we use both a pulsed UV laser system with a near Fourier-transform-limited bandwidth of 150 MHz [depicted in Fig. 3a)] and a continuous-wave (cw) single-mode UV laser with a bandwidth of 1.5 MHz [depicted in Fig. 3c)]. To generate the pulsed UV radiation, the cw output of a ring dye laser with a wavelength around 580 nm is pulse amplified in dye cells pumped with the second harmonic of a neodymium-doped yttrium-aluminium-garnet (Nd:YAG) laser and frequency doubled in a beta-barium-borate (BBO) crystal. The pulse amplified fundamental radiation is frequency calibrated to an accuracy of 20 MHz (1σ) with a wave meter and a fraction of the cw output of the ring dye laser is used to record the laser-induced-fluorescence spectrum of I_2, as desribed in Ref. [17]. The difference between the frequencies of the cw and pulse-amplified outputs of the ring-dye laser is used to quantify the effects of the frequency chirp arising in the pulse-amplification process. The experiments involving cw UV radiation made use of the cw output of the ring laser, which was frequency doubled in an external cavity. In the experiments involving cw radiation, only the relative frequency was measured with an etalon

at an accuracy of 5 MHz.

A supersonic beam of metastable helium molecules is produced in an electric discharge through an expansion of pure helium gas [13] in a source chamber. The body of the valve can be cooled to temperatures of 77 and 10 K, resulting in supersonic beams with velocities of approximately 1000 and 500 m/s, respectively [19]. The molecular beam is collimated with a skimmer before entering a second, differentially-pumped vacuum chamber that contains a 55-coil multistage Zeeman decelerator [18, 19, 61].

The Zeeman decelerator exploits the Zeeman effect to manipulate the longitudinal velocity of the metastable helium molecules. When a He_2^* molecule approaches an inhomogeneous magnetic field, it experiences a force that depends on its effective dipole moment. In a magnetic field, the $J'' = 2$ fine-structure component of the $N'' = 1$ rotational ground state of He_2^* is split into five magnetic sublevels that are labeled with their value of $M_{J''}$, the quantum number associated with the projection of the total angular momentum vector J'' on the magnetic-field axis (see Fig. 1). The energy of two of the five magnetic sublevels increases as the magnetic-field strength increases. Molecules in these two states experience a force toward regions of low magnetic-field strength and are therefore referred to as "low-field seekers". Analogously, molecules in a state that displays a decrease in energy with increasing magnetic-field strength experience a force toward regions of high magnetic-field strength and are referred to as a "high-field seekers". When a low-field seeker approaches a magnetic field that is created by applying a current to a solenoid, part of its kinetic energy is converted into Zeeman energy and the molecule slows down. However, as soon as the low-field seeker crosses the region of maximum magnetic field, corresponding to the center of the solenoid, it gets accelerated again. In order to prevent this reacceleration, the magnetic field is switched off abruptly. By repeating this process many times and choosing the switch-off time of the current in the solenoids so as to maintain a phase-stable deceleration [62], the molecules can be decelerated to any desired velocity. Because the magnetic field has to be switched off before the molecule leaves the coil, the maximum velocity that can

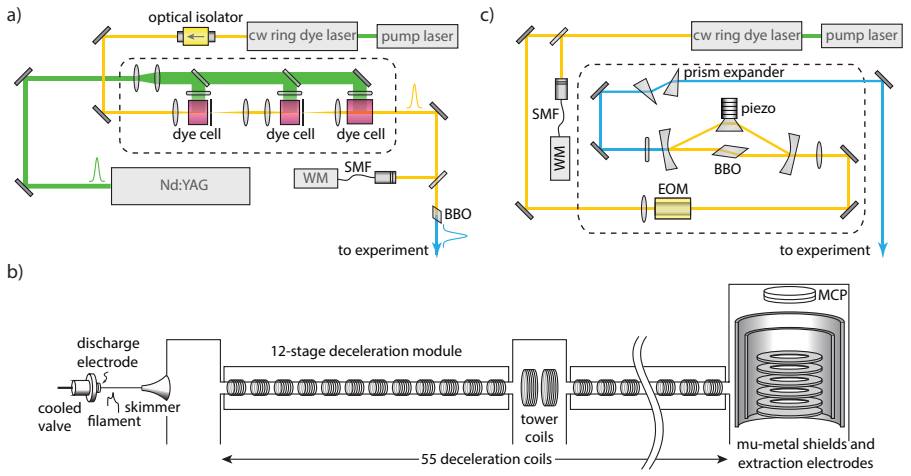

Figure 3: Schematic representation (not to scale) of the experimental setup. a) pulsed-amplified ring-dye laser, b) vacuum setup showing the discharge source, the Zeeman decelerator, and the magnetically shielded photoexcitation region, and c) cw doubling of the output of a ring dye laser using a cavity. Nd:YAG, neodymium-doped yttrium aluminum garnet; WM, wave meter; SMF, single mode fiber; BBO, beta barium borate crystal; MCP, microchannel plate detector.

be manipulated by a single coil is determined by the ratio of the length of the coil and the switch-off time of the magnetic field. For our experimental parameters (7.2 mm, 8 μs, 250 A, and maximal on-axis field strength of 2 T) this results in a maximum velocity around 700 m/s. To obtain an initial velocity below this value, the valve body has to be cooled to 10 K.

The decelerator is segmented into three modules: two modules containing 12 coils and one module containing 31 coils. These modules are separated by pumping towers to guarantee a low background pressure in the decelerator. In addition, the modular design of the decelerator offers the flexibility to match the number of coils to the magnetic-moment-to-mass ratio of the species of interest. In order to maintain the magnetic quantization axis of the molecules as they traverse the region between the deceleration modules, the towers are equipped with solenoids as well, as explained by Wiederkehr *et al.* [61].

After about 1 m of flight, the molecules enter a third vacuum chamber that is

used for photoexcitation and detection. Approximately 60 mm beyond the last coil of the decelerator, the molecular beam is intersected at right angles with the UV laser beam that is used to drive transitions to np Rydberg states. The excitation region is surrounded by a cylindrically symmetric stack of electrodes for the application of ionization and extraction electric fields. A weak dc electric field is applied to the stack during photoexcitation in order to reduce stray electric fields to below 1 mV/cm. The stray field is determined by recording spectra in the presence of different dc electric fields and fitting the observed Stark shifts to a quadratic polynomial, as illustrated in Fig. 4. In order to suppress stray magnetic fields, two concentric mu-metal tubes are used to shield the excitation region. For molecules decelerated to 120 m/s, the current in the last coil is switched off 0.5 ms before the molecules reach the excitation volume. The Rydberg states are ionized for detection by the application of a pulsed electric field which is also used to extract the ions toward a microchannel-plate (MCP) detector. A small electric field is applied to the stack shortly after photoexcitation but before the ionization pulse. This discrimination pulse separates prompt ions, produced by direct ionization or rapid autoionization, from ions produced by pulsed field ionization, based on their different arrival times on the MCP detector. The discrimination pulse also induces the field ionization of Rydberg states with $n \gtrsim 200$, so that these states contribute to the prompt-ion signal.

4. Results

The procedure for obtaining the intervals between successive rotational states in He_2^+ relies on the determination of the relative convergence limits of Rydberg series excited by Q-type and O-type transitions. This procedure has been used to extract the interval $\tilde{\nu}_{31}^+$ between the $N^+ = 1$ and $N^+ = 3$ rotational levels of He_2^+ in Ref. [17] and is briefly repeated here. $\tilde{\nu}_{31}^+$ corresponds to the difference between the convergence limits $\tilde{\nu}_{13}$ of the $3 \rightarrow n\mathrm{p}1_2$ series and $\tilde{\nu}_{33}$ of the $3 \rightarrow n\mathrm{p}3_3$ series (see Fig. 2). This interval can also be determined from the

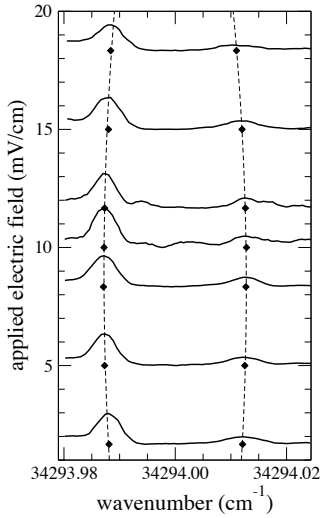

Figure 4: Spectra of the $1_1 \rightarrow 123p1_2$ transition (left-hand side) and $1_0 \rightarrow 124p1_1$ transition (right-hand side) of He_2^* recorded in the presence of different dc electric fields. The vertical shift of the baseline of each spectrum corresponds to the applied field in units of mV/cm. The diamonds show the transition frequencies and the dashed lines represent fits using quadratic polynomials. In this way, the stray field could be reduced to below 1 mV/cm.

convergence limits $\tilde{\nu}_{11}$ of the $1 \rightarrow np1_{0-2}$ series and $\tilde{\nu}_{33}$ of the $3 \rightarrow np3_3$ series in combination with the interval $\tilde{\nu}''_{31}$ between the $N'' = 1$ and $N'' = 3$ rotational levels of He_2^* and is given by $\tilde{\nu}^+_{13} = \tilde{\nu}''_{31} + \tilde{\nu}_{33} - \tilde{\nu}_{11}$. In order to derive the $\tilde{\nu}''_{31}$ interval, differences between transition wave numbers from $N'' = 1$ and $N'' = 3$ rotational levels to any member of the $np1_2$ series can be taken. This procedure is illustrated in Fig. 5 that shows the $1 \rightarrow np1_{1,2}$ and $3 \rightarrow np1_2$ Rydberg series around $n = 128$ [17]. To account for the triplet structure of the initial states, three Gaussian profiles have been fitted to the observed line shapes. The energy splitting between the line centers is fixed to the known fine-structure intervals [45] and the relative intensities are assumed to correspond to the degeneracy factors $2J'' + 1$. The interval between the $N'' = 1$ and 3 rotational levels of He_2^* was determined to be $75.8137(4)\,\mathrm{cm}^{-1}$ [17], in agreement with the value of $75.8129(3)\,\mathrm{cm}^{-1}$ derived from the rotational Hamiltonian and molecular constants reported by Focsa *et al.* [36].

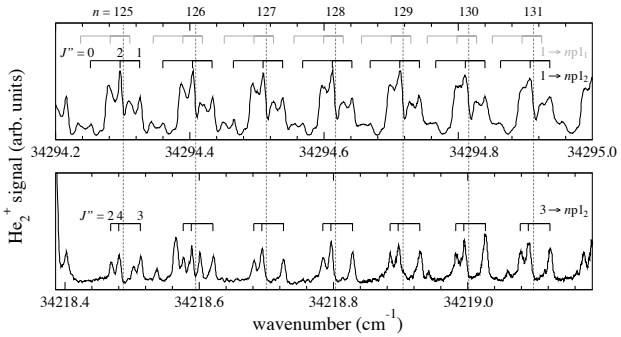

Figure 5: Determination of the $\tilde{\nu}_{31}''$ interval between the N'' = 1 and 3 rotational levels of He_2^* from combinational differences of transitions converging on the same np1$_2$ Rydberg level. Vertical dashed lines indicate the centers of gravity of the transitions.

The convergence limits of the Rydberg series were derived by extrapolating transitions to Rydberg states of principal quantum numbers in the range $n = 95 - 115$. This choice represents a compromise between states that are high enough in n for the uncertainties in the quantum defects to have a negligible effect on the extrapolated energies and low enough not to be strongly affected by the Stark effect. The ionization thresholds $\tilde{\nu}_{11}, \tilde{\nu}_{13}$ and $\tilde{\nu}_{33}$ were determined to be 34301.20585(10), 34225.39234(10), and 34296.33037(7) cm^{-1}, respectively, with a systematic uncertainty of 1.4×10^{-3} cm^{-1} [17]. The lowest rotational interval in He_2^+ was thus determined to be 70.9380(6) cm^{-1} with a total uncertainty of 6×10^{-4} cm^{-1} or 18 MHz, which is less than the estimated uncertainty ($\approx 4 \times 10^{-3}$ cm^{-1}) of the most recent and precise theoretical value [9].

Higher rotational intervals of He_2^+ can be determined by recording Rydberg series that converge on higher-rotational states of the ion. As an example, spectra of the 13 $\rightarrow$ np11$_{12}$ Rydberg series in the range $n \approx 60 - 67$ and 13 $\rightarrow$ np13$_{13,14}$ Rydberg series in the range $n \approx 95 - 115$ are shown in Fig. 6(a) and (b), respectively. The spectra also contain spectral features that correspond to transitions of the 1 $\rightarrow$ np1$_{1,2}$ to 11 $\rightarrow$ np11$_{11,12}$ series. The energy interval between the N^+ = 11 and 13 rotational states in He_2^+ can be estimated by taking the difference between the series limits extrapolated using Rydberg's

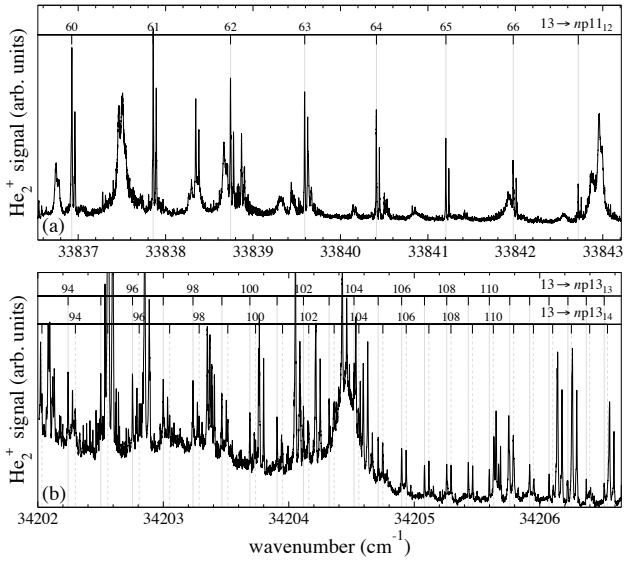

Figure 6: Rydberg spectra of the (a) $13 \rightarrow n\mathrm{p}11_{12}$ series of He_2 in the range $n \approx 60 - 67$ and (b) $13 \rightarrow n\mathrm{p}13_{13,14}$ series in the range $n \approx 95 - 115$. The spectra also contain contributions from transitions belonging to $1 \rightarrow n\mathrm{p}1_{1,2}$ to $11 \rightarrow n\mathrm{p}11_{11,12}$ Rydberg series.

formula. Setting the uncertainty equal to the experimental linewidth, we determine this interval to be $346.988(6)\,\mathrm{cm}^{-1}$, as compared to the theoretical value of $346.977(4)\,\mathrm{cm}^{-1}$ [9]. Extrapolation of the $13 \rightarrow n\mathrm{p}11_{12}$ and $13 \rightarrow n\mathrm{p}13_{13,14}$ Rydberg series using MQDT should result in a more accurate determination of the $N^+ = 11$-to-13 rotational interval in He_2^+. However, an accurate determination by MQDT requires the precise knowledge of higher rotational levels of He_2^+, which is not available yet but can be obtained in a global analysis of all measured O-type and Q-type transitions to Rydberg states. Such an analysis is currently being performed, including series converging to rotational levels of He_2^+ as high as $N^+ = 21$ [63].

An important asset of the experiment is the use of a multistage Zeeman decelerator to reduce the velocity of the beam of metastable helium molecules and, consequently, systematic Doppler *shifts* resulting from the velocity components parallel to the laser beam. In Fig. 7, traces (a) and (b) show part of

the Rydberg spectrum of He_2^* in the vicinity of the $1 \rightarrow 94p1_{1,2}$ transition that was obtained using an undecelerated beam with a velocity of 1000 m/s and a decelerated beam with a velocity of 120 m/s, respectively. Many lines that are present in the spectrum recorded with the undecelerated beam are not observed in the spectrum obtained with the decelerated beam. This reduction in spectral congestion is a consequence of the spin-rotational state selectivity of the deceleration process. As expected from the Zeeman map of Fig. 1, the $J'' = N''$ component is completely rejected from the beam, and transitions originating from this level are absent after deceleration. In addition, the $J'' = 2$ component carries approximately half the intensity of the $J'' = 0$ component for the Q(1)-type transitions and in the case of the Q(3)-type transitions, the $J'' = 4$ component is hardly visible in the spectrum and only the $J'' = 2$ component is observed. From the Zeeman map of He_2^* shown in Fig. 1, one would expect that the relative intensities of the $J'' = 0$ and 2, and $J'' = 2$ and 4 fine-structure states would reflect the respective number of low-field seeking states, that is, one would expect ratios of 1:2 and 5:2, respectively, in contrast to the ratios of 2:1 and >20:1 observed experimentally.

The apparent loss of molecules in the $J'' = N'' + 1$ fine-structure component during the deceleration process can be understood in terms of a redistribution over all $M_{J''}$ states in regions of near-zero magnetic-field strength in the pumping towers. Although the pumping towers are equipped with coils that are pulsed as the molecules pass, the generated magnetic field is not strong enough in this case to maintain the magnetic quantization axis over the whole tower region, resulting in nonadiabatic losses. Assuming a complete redistribution over all $M_{J''}$ states every time the molecules traverse a tower, one expects the population of the $J'' = 2$ and 4 components to be suppressed by factors of $(5/2)^\tau$ and $(9/2)^\tau$, respectively, where τ is the number of towers the molecules traverse. The spectra in Fig. 7 have been normalized with respect to the $J'' = 0$ fine-structure component of the transition to the $94np1_2$ Rydberg state and vertical bars indicate the expected intensities of the fine-structure components with respect to the $J'' = N'' - 1$ state, assuming a complete redistribution over $M_{J''}$ states for

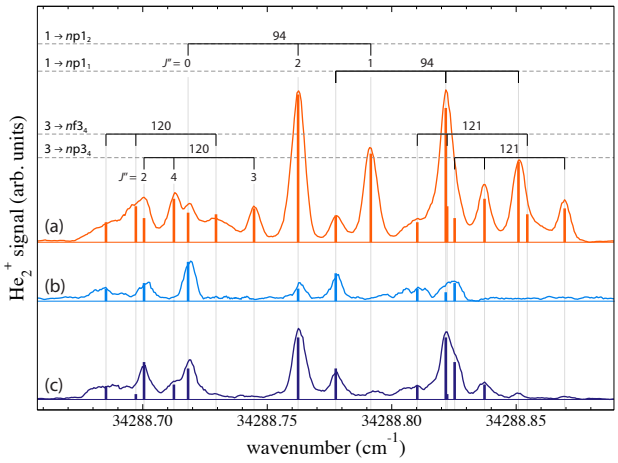

Figure 7: Comparison between relative intensities of rotational fine structure components for spectra obtained from nondecelerated samples of He_2^* [1000 m/s, trace (a)], a spectrum obtained from a sample decelerated from 500 to 120 m/s using three deceleration modules and two pumping towers [trace (b)], and a spectrum obtained from a sample decelerated from 500 to 335 m/s using a single 31-stage deceleration module without any tower [trace (c)]. Vertical bars indicate expected relative line intensities based on the Zeeman energy of the different $M_{J''}$ states and assuming a complete redistribution among near-degenerate $M_{J''}$ levels. Note that for trace (c) the decelerated and undecelerated molecules are not completely separated spatially, giving rise to small features from the $J'' = N''$ fine-structure components.

the decelerated sample with $\tau = 2$. Trace (c) in Fig. 7 displays the same spectral region but was obtained using a molecular beam that was decelerated from 500 to 335 m/s using a single 31-stage deceleration module without any tower ($\tau = 0$). The relative intensities of the fine-structure components in this spectrum exactly matches the number of low-field seeking states. The observed changes of intensities resulting from $M_{J''}$ redistribution processes confirm the validity of the assumption of a statistical redistribution among the near-degenerate magnetic sublevels at each tower. These $M_{J''}$ redistribution processes actually turn out to be a powerful tool to assign transitions to specific initial N'', J'' levels.

Figure 7 also indicates that no residual Doppler *shifts* persist within the statistical uncertainty of the measurements. In principle, a reduction of the beam velocity results in a reduction of the Doppler *width* of spectral lines and should

therefore allow for a more precise determination of observed spectral positions. However, the pulse-amplification process results in a spectral resolution that is limited by the pulse width of the pumping laser. Assuming a Fourier-transform-limited Gaussian pulse with a pulse duration of 4 ns, the frequency-doubled output of the laser has a bandwidth of about 150 MHz. Because this bandwidth is larger than the Doppler width, no reduction of the line widths was observed for decelerated molecules. In order to observe an effect of the beam velocity on the Doppler width of the measured transitions, the bandwidth of the laser system has to be reduced below the Doppler linewidth. Because of the inherent limitations of a pulsed-laser system, this can be best achieved by replacing the pulsed laser by a cw laser, as shown in Fig. 3c).

As an example, the $1_2 \rightarrow 51n\mathrm{p}1_2$ transition, obtained using the cw laser system presented in Fig. 3c), is shown in Fig. 8, however, without pulsing currents through the deceleration coils. The red triangles and blue diamonds represent measurements with the valve body kept at a temperature of 77 and 10 K, respectively. The red and blue curves are Gaussian fits to the data and have a full width at half maximum (FWHM) of 50 and 25 MHz, respectively. The decrease of the linewidth by a factor of two reflects the reduction in velocity from 1000 to 500 m/s for the lower temperature. It is expected that decelerating the molecules to velocities around 100 m/s will result in a further reduction of the observed linewidths, and work in this direction is currently in progress.

5. Conclusions

High-resolution spectroscopy of high Rydberg states of He_2 using a pulsed UV laser with a Fourier-transform-limited bandwidth of 150 MHz was used to determine energy intervals between rotational states of ${He_2}^+$, the $N^+ = 1$ to $N^+ = 3$ interval with a precision of 18 MHz and the $N^+ = 11$ to the $N^+ = 13$ interval with a precision of 150 MHz. Both intervals are smaller than predicted by the most recent *ab initio* calculations [9], which do not include QED corrections to the level energies.

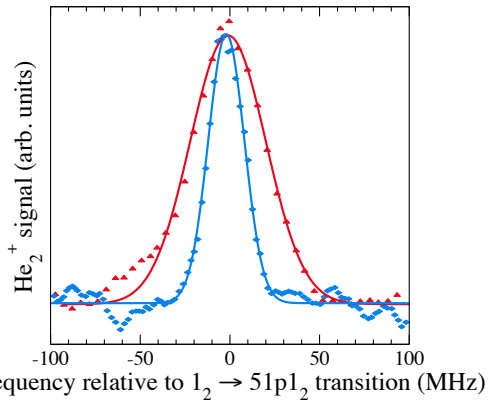

Figure 8: Comparison between measurements of the $1_2 \rightarrow 51p1_2$ transition using the cw ring dye laser setup of Fig. 3c) with valve temperatures of 77 (solid triangles) and 10 K (solid diamonds), respectively. The solid red and blue lines represent gaussian fits to the data points with FWHM's of 50, and 25 MHz, respectively.

Multistage Zeeman deceleration was used to generate slow beams of translationally cold metastable He_2 molecules (He_2^*) and contributed to a reduction of the uncertainties in the experimental transition frequencies by reducing Doppler shifts. A complete redistribution among near-degenerate magnetic sublevels of the spin-rotational levels of metastable He_2 in regions of near-zero magnetic fields located in the pumping sections of the decelerator was shown to affect the relative populations of the N'', J'' spin-rotational states of He_2^*, and, by doing so, facilitated the spectral assignments.

Replacing the pulsed UV laser by a cw UV laser enabled us to reduce the line widths of the observed transitions from 150 MHz to 50 and 25 MHz in experiments carried out with He_2^* beams having average velocities of 1000 and 500 m/s, respectively. The combination of multistage Zeeman deceleration of He_2^* with cw-laser excitation has the potential to improve the precision and accuracy of the present results by more than an order of magnitude, as recently demonstrated using an ultracold sample of cesium atoms in Ref. [64].

Acknowledgment

We thank Hansjürg Schmutz and Josef Agner for their expert technical assistance. This work is supported financially by the Swiss National Science Foundation under Project No. 200020-159848 and the NCCR QSIT. P. J. acknowledges ETH Zurich for support through an ETH fellowship.

References

References

[1] T. Steimle, W. Ubachs, Introduction to the Special issue Spectroscopic Tests of Fundamental Physics, J. Mol. Spectrosc. 300 (2014) 1–2. doi:10.1016/j.jms.2014.04.004.

[2] V. I. Korobov, Leading-order relativistic and radiative corrections to the rovibrational spectrum of H_2^+ and HD^+ molecular ions, Phys. Rev. A 74 (5) (2006) 052506. doi:10.1103/PhysRevA.74.052506.

[3] V. I. Korobov, Relativistic corrections of $m\alpha^6$ order to the rovibrational spectrum of H_2^+ and HD^+ molecular ions, Phys. Rev. A 77 (2) (2008) 022509. doi:10.1103/PhysRevA.77.022509.

[4] K. Piszczatowski, G. Łach, M. Przybytek, J. Komasa, K. Pachucki, B. Jeziorski, Theoretical Determination of the Dissociation Energy of Molecular Hydrogen, J. Chem. Theory Comput. 5 (11) (2009) 3039–3048. doi:10.1021/ct900391p.

[5] K. Pachucki, J. Komasa, Rovibrational levels of HD, Phys. Chem. Chem. Phys. 12 (32) (2010) 9188–9196. doi:10.1039/C0CP00209G.

[6] V. I. Korobov, L. Hilico, J.-P. Karr, Theoretical transition frequencies beyond 0.1 ppb accuracy in H_2^+, HD^+, and antiprotonic helium, Phys. Rev. A 89 (3) (2014) 032511. doi:10.1103/PhysRevA.89.032511.

[7] J. Liu, E. J. Salumbides, U. Hollenstein, J. C. J. Koelemeij, K. S. E. Eikema, W. Ubachs, F. Merkt, Determination of the ionization and dissociation energies of the hydrogen molecule, J. Chem. Phys. 130 (17) (2009) 174306. doi:10.1063/1.3120443.

[8] D. Sprecher, C. Jungen, W. Ubachs, F. Merkt, Towards measuring the ionisation and dissociation energies of molecular hydrogen with sub-MHz accuracy, Faraday Discuss. 150 (2011) 51–70. doi:10.1039/C0FD00035C.

[9] W.-C. Tung, M. Pavanello, L. Adamowicz, Very accurate potential energy curve of the He_2^+ ion, J. Chem. Phys. 136 (10) (2012) 104309. doi:10.1063/1.3692800.

[10] N. Yu, W. H. Wing, Observation of the infrared spectrum of the helium molecular ion $(^3He^4He)^+$, Phys. Rev. Lett. 59 (18) (1987) 2055–2058. doi:10.1103/PhysRevLett.59.2055.

[11] N. Yu, W. H. Wing, L. Adamowicz, Hyperfine structure in the infrared spectrum of $^3He^4He^+$, Phys. Rev. Lett. 62 (3) (1989) 253–256. doi:10.1103/PhysRevLett.62.253.

[12] A. Carrington, C. H. Pyne, P. J. Knowles, Microwave electronic spectrum of the He_2^+ ion, J. Chem. Phys. 102 (15) (1995) 5979–5988. doi:10.1063/1.469332.

[13] M. Raunhardt, M. Schäfer, N. Vanhaecke, F. Merkt, Pulsed-field-ionization zero-kinetic-energy photoelectron spectroscopy of metastable He_2: Ionization potential and rovibrational structure of He_2^+, J. Chem. Phys. 128 (16) (2008) 164310. doi:10.1063/1.2904563.

[14] D. S. Ginter, M. L. Ginter, The spectrum and structure of the He_2 molecule: Multichannel quantum defect analyses of the triplet levels associated with $(1\sigma_g)^2(1\sigma_u)np\lambda$, J. Mol. Spectrosc. 82 (1) (1980) 152–175. doi:10.1016/0022-2852(80)90106-X.

[15] D. S. Ginter, M. L. Ginter, C. M. Brown, Multichannel interactions in the $(1\sigma_g)^2(1\sigma_u)n\mathrm{p}\lambda(^3\Pi_g,\ ^3\Sigma_g^+)$ Rydberg structures of He_2, J. Chem. Phys. 81 (12) (1984) 6013–6025. doi:10.1063/1.447603.

[16] D. Sprecher, J. Liu, T. Krähenmann, M. Schäfer, F. Merkt, High-resolution spectroscopy and quantum-defect model for the gerade triplet np and nf Rydberg states of He_2, J. Chem. Phys. 140 (6) (2014) 064304. doi:10.1063/1.4864002.

[17] P. Jansen, L. Semeria, L. E. Hofer, S. Scheidegger, J. A. Agner, H. Schmutz, F. Merkt, Precision Spectroscopy in Cold Molecules: The Lowest Rotational Interval of He_2^+ and Metastable He_2, Phys. Rev. Lett. 115 (13) (2015) 133202. doi:10.1103/PhysRevLett.115.133202.

[18] N. Vanhaecke, U. Meier, M. Andrist, B. H. Meier, F. Merkt, Multistage Zeeman deceleration of hydrogen atoms, Phys. Rev. A 75 (2007) 031402. doi:10.1103/PhysRevA.75.031402.
URL http://link.aps.org/doi/10.1103/PhysRevA.75.031402

[19] M. Motsch, P. Jansen, J. A. Agner, H. Schmutz, F. Merkt, Slow and velocity-tunable beams of metastable He_2 by multistage Zeeman deceleration, Phys. Rev. A 89 (4) (2014) 043420. doi:10.1103/PhysRevA.89.043420.

[20] D. Sprecher, M. Beyer, F. Merkt, Precision measurement of the ionisation energy of the $3\mathrm{d}\sigma$ GK state of H_2, Mol. Phys. 111 (14-15) (2013) 2100–2107. arXiv:http://dx.doi.org/10.1080/00268976.2013.788743, doi:10.1080/00268976.2013.788743.
URL http://dx.doi.org/10.1080/00268976.2013.788743

[21] W. E. Curtis, A New Band Spectrum Associated with Helium, Proc. R. Soc. A 89 (608) (1913) 146–149.
URL http://www.jstor.org/stable/93468

[22] E. Goldstein, Über ein noch nicht beschriebenes, anscheinend dem Helium angehörendes Spektrum, Verh. Dtsch. Phys. Ges. 15 (1913) 402–412.

[23] M. L. Ginter, Spectrum and Structure of the He_2 Molecule. I. Characterization of the States Associated with the UAO's 3pσ and 2s, J. Chem. Phys. 42 (2) (1965) 561–568. doi:10.1063/1.1695973.

[24] M. L. Ginter, The spectrum and structure of the He_2 molecule: Part II. Characterization of the singlet states associated with the UAO's 3s and 2pπ, J. Mol. Spectrosc. 17 (2) (1965) 224–239. doi:10.1016/0022-2852(65)90162-1.

[25] M. L. Ginter, The spectrum and structure of the He_2 molecule: Part III. Characterization of the triplet states associated with the UAO's 3s and 2pπ, J. Mol. Spectrosc. 18 (3) (1965) 321–343. doi:10.1016/0022-2852(65)90143-8.

[26] M. L. Ginter, Spectrum and Structure of the He_2 Molecule. IV. Characterization of the Singlet and Triplet States Associated with the UAO's 3dσ, 3dπ, and 3dδ, J. Chem. Phys. 45 (1) (1966) 248–262. doi:10.1063/1.1727318.

[27] M. L. Ginter, D. S. Ginter, Spectrum and Structure of the He_2 Molecule. V. Characterization of the Triplet States Associated with the UAO's $6-17\,\mathrm{p}\pi$ and $7-12\,\mathrm{p}\sigma$, J. Chem. Phys. 48 (5) (1968) 2284–2291. doi:10.1063/1.1669426.

[28] M. L. Ginter, R. Battino, Potential-Energy Curves for the He_2 Molecule, J. Chem. Phys. 52 (9) (1970) 4469–4474. doi:10.1063/1.1673675.

[29] C. M. Brown, M. L. Ginter, Spectrum and structure of the He_2 molecule VI. Characterization of the states associated with the UAO's 3pπ and 2s, J. Mol. Spectrosc. 40 (2) (1971) 302–316. doi:10.1016/0022-2852(71)90156-1.

[30] D. S. Ginter, M. L. Ginter, Spectrum and structure of the He_2 molecule: Characterization of the triplet states associated with $(1\sigma_g)^2(1\sigma_u)ns\sigma$, $n\mathrm{d}\sigma$, $n\mathrm{d}\pi$, and $n\mathrm{d}\delta$ $(n = 5-12)$, J. Mol. Spectrosc. 101 (1) (1983) 139–160. doi:10.1016/0022-2852(83)90012-7.

[31] G. Hepner, L. Herman, Nouveau système de bandes d'émission de la molécule He_2 vers 4700 cm^{-1}, CR Acad Sci Paris Ser B 243 (20) (1956) 1504–1506.

[32] P. Gloersen, G. H. Dieke, Molecular spectra of hydrogen and helium in the infrared, J. Mol. Spectrosc. 16 (1) (1965) 191–204. doi:10.1016/0022-2852(65)90097-4.

[33] T. A. Miller, V. E. Bondybey, Laser excitation spectra of He_2, J. Mol. Spectrosc. 78 (1) (1979) 120–124. doi:10.1016/0022-2852(79)90039-0.

[34] S. A. Rogers, C. R. Brazier, P. F. Bernath, J. W. Brault, Fourier transform emission spectroscopy of the $b\,^3\Pi_g - a\,^3\Sigma_u^+$ transition of He_2, Mol. Phys. 63 (5) (1988) 901–908. doi:10.1080/00268978800100641.

[35] G. Herzberg, C. Jungen, The 4f states of He_2: A new spectrum of He_2 in the near infrared, J. Chem. Phys. 84 (3) (1986) 1181–1192. doi:10.1063/1.450509.

[36] C. Focsa, P. F. Bernath, R. Colin, The Low-Lying States of He_2, J. Mol. Spectrosc. 191 (1) (1998) 209–214. doi:10.1006/jmsp.1998.7637.

[37] Y. Hosaki, S. Civiš, K. Kawaguchi, Time-resolved Fourier transform infrared emission spectroscopy of He_2 produced by a pulsed discharge, Chem. Phys. Lett. 383 (3–4) (2004) 256–260. doi:10.1016/j.cplett.2003.11.025.

[38] H. Solka, W. Zimmermann, A. Stahn, D. Reinert, W. Urban, Observation of the $B\,^1\Pi_g - A\,^1\Sigma_u^+$ band of He_2, Mol. Phys. 60 (5) (1987) 1179–1182. doi:10.1080/00268978700100781.

[39] K. Kawakita, K. Fukuda, Y. Adachi, C. Hirose, Doppler-free optogalvanic spectrum of He_2 $b\,^3\Pi_g - f\,^3\Delta_u$ transition, J. Chem. Phys. 82 (2) (1985) 653–657. doi:10.1063/1.448540.

[40] D. C. Lorents, S. Keiding, N. Bjerre, Barrier tunneling in the He_2 $c\,^3\Sigma_g^+$ state, J. Chem. Phys. 90 (6) (1989) 3096–3101. doi:10.1063/1.455912.

[41] I. Hazell, A. Norregaard, N. Bjerre, Highly Excited Rotational and Vibrational Levels of the Lowest Triplet States of He_2: Level Positions and Fine Structure, J. Mol. Spectrosc. 172 (1) (1995) 135–152. doi:10.1006/jmsp.1995.1162.

[42] C. Li, L. Deng, J. Zhang, X. Yang, Y. Chen, L. Ma, The absorption spectrum of the (1, 0), (3, 1) and (4, 2) bands in the $c\,^3\Sigma_g^+ - a\,^3\Sigma_u^+$ system of He_2 eximer, J. Mol. Spectrosc. 260 (2) (2010) 85–87. doi:10.1016/j.jms.2009.12.002.

[43] R. L. Brooks, J. L. Hunt, Helium emission spectra from doped samples of solid hydrogen and deuterium, J. Chem. Phys. 88 (12) (1988) 7267–7272. doi:10.1063/1.454337.

[44] D. W. Tokaryk, G. R. Wagner, R. L. Brooks, J. L. Hunt, Infrared emission spectra from cryogenic proton-irradiated helium gas, J. Chem. Phys. 103 (24) (1995) 10439–10444. doi:10.1063/1.469893.

[45] W. Lichten, M. V. McCusker, T. L. Vierima, Fine structure of the metastable $a\,^3\Sigma_u^+$ state of the helium molecule, J. Chem. Phys. 61 (6) (1974) 2200–2212. doi:10.1063/1.1682292.

[46] T. L. Vierima, Determination of the sign of the spin–spin interaction in $He_2(a\,^3\Sigma_u^+)$, J. Chem. Phys. 62 (7) (1975) 2925–2926. doi:10.1063/1.430803.

[47] W. Lichten, T. Wik, Fine structure of the metastable $a\,^3\Sigma_u^+$ state of the helium molecule. Further results, J. Chem. Phys. 69 (1) (1978) 98–100. doi:10.1063/1.436350.

[48] M. Kristensen, N. Bjerre, Fine structure of the lowest triplet states in He_2, J. Chem. Phys. 93 (2) (1990) 983–990. doi:10.1063/1.459125.

[49] W. Cencek, M. Przybytek, J. Komasa, J. B. Mehl, B. Jeziorski, K. Szalewicz, Effects of adiabatic, relativistic, and quantum electrodynamics interactions on the pair potential and thermophysical properties of helium, J. Chem. Phys. 136 (22) (2012) 224303. doi:10.1063/1.4712218.

[50] R. E. Grisenti, W. Schöllkopf, J. P. Toennies, G. C. Hegerfeldt, T. Köhler, M. Stoll, Determination of the Bond Length and Binding Energy of the Helium Dimer by Diffraction from a Transmission Grating, Phys. Rev. Lett. 85 (11) (2000) 2284–2287. doi:10.1103/PhysRevLett.85.2284.

[51] M. L. Ginter, in: B. Rosen (Ed.), Données Spectroscopiques Relatives aux Molécules Diatomiques, Pergamonn Press, Oxford, 1970.

[52] K. P. Huber, G. Herzberg, Molecular Spectra And Molecular Structure, IV. Constants Of Diatomic Molecules, Van Nostrand Reinhold Company, New York, 1979.
URL http://archive.org/details/ MolecularSpectraAndMolecularStructureIV.ConstantsOfDiat

[53] G. Herzberg, Rydberg Molecules, Annu. Rev. Phys. Chem. 38 (1) (1987) 27–56. doi:10.1146/annurev.pc.38.100187.000331.

[54] C. F. Chabalowski, J. O. Jensen, David R. Yarkony, B. H. Lengsfield III, Theoretical study of the radiative lifetime for the spin-forbidden transition $a\,^3\Sigma_u^+ \rightarrow X\,^1\Sigma_g^+$ in He_2, J. Chem. Phys. 90 (4) (1989) 2504–2512. doi:10.1063/1.455993.

[55] H. Lefebvre-Brion, R. W. Field, The Spectra and Dynamics of Diatomic Molecules, Academic Press, San Diego, 2004.
URL http://www.sciencedirect.com/science/article/pii/B9780124414556500007

[56] J. M. Brown, A. Carrington, Rotational Spectroscopy of Diatomic Molecules, Cambridge University Press, Cambridge, 2003.
URL http://ebooks.cambridge.org/ref/id/CBO9780511814808

[57] J. M. Brown, J. K. G. Watson, Spin-orbit and spin-rotation coupling in doublet states of diatomic molecules, J. Mol. Spectrosc. 65 (1) (1977) 65–74. doi:10.1016/0022-2852(77)90358-7.

[58] C. Jungen, Elements of Quantum Defect Theory, in: Handbook of High-resolution Spectroscopy, Vol. 1, John Wiley & Sons, 2011.

URL http://onlinelibrary.wiley.com/doi/10.1002/9780470749593.hrs024/abstract

[59] C. Haase, M. Beyer, C. Jungen, F. Merkt, The fundamental rotational interval of para-H_2^+ by MQDT-assisted Rydberg spectroscopy of H_2, J. Chem. Phys. 142 (6) (2015) 064310. doi:10.1063/1.4907531.

[60] S. Willitsch, F. Merkt, Rovibronic photoionization dynamics of asymmetric-top molecules, Int. J. Mass Spectrom. 245 (1–3) (2005) 14–25. doi:10.1016/j.ijms.2005.06.004.

[61] A. W. Wiederkehr, M. Motsch, S. D. Hogan, M. Andrist, H. Schmutz, B. Lambillotte, J. A. Agner, F. Merkt, Multistage Zeeman deceleration of metastable neon, J. Chem. Phys. 135 (21) (2011) 214202. doi:10.1063/1.3662141.

[62] A. W. Wiederkehr, S. D. Hogan, F. Merkt, Phase stability in a multistage zeeman decelerator, Phys. Rev. A 82 (2010) 043428. doi:10.1103/PhysRevA.82.043428.
URL http://link.aps.org/doi/10.1103/PhysRevA.82.043428

[63] L. Semeria, P. Jansen, F. Merkt, unpublished results.

[64] J. Deiglmayr, H. Herburger, H. Saßmannshausen, P. Jansen, H. Schmutz, F. Merkt, Precision measurement of the ionization energy of Cs I, ACCEPTED FOR PUBLICATION IN PHYS. REV. A.
URL HTTPS://JOURNALS.APS.ORG/PRA/ACCEPTED/53076N80X301B11095C405773133B29891BF5127E